HHS Public Access

Author manuscript

Adv Mater. Author manuscript; available in PMC 2024 December 01.

Published in final edited form as:

Adv Mater. 2023 December ; 35(49): e2304049. doi:10.1002/adma.202304049.

Exploring the Role of Spatial Confinement in Immune Cell Recruitment and Regeneration of Skin Wounds

Dr. Yining Liu[1], **Alejandra Suarez-Arnedo**[1], **Eleanor L.P. Caston**[1], **Dr. Lindsay Riley**[1], **Dr. Michelle Schneider**[2], **Prof. Tatiana Segura**[1,3,*]

[1]Department of Biomedical Engineering, Duke University, 101 Science Drive Campus Box 90281, Durham, NC 27708, USA

[2]Department of Pathology, Duke University School of Medicine, Durham, NC 27710, USA

[3]Clinical Science Departments of Neurology and Dermatology, Duke University, Durham, NC 27708, USA

Abstract

Microporous annealed particle (MAP) scaffolds are injectable granular materials comprised of micron sized hydrogel particles (microgels). The diameter of these microgels directly determines the size of the interconnected void space between particles where infiltrating or encapsulated cells reside. This tunable porosity allows us to use MAP scaffolds to study the impact of spatial confinement (SC) on both cellular behaviors and the host response to biomaterials. Despite previous studies showing that pore size and SC influence cellular phenotypes, including mitigating the macrophage inflammatory response, there is still a gap in knowledge regarding how SC within a biomaterial modulates immune cell recruitment *in vivo* in wounds and implants. Thus, we studied the immune cell profile within confined and unconfined biomaterials using small (40 μm), medium (70 μm), and large (130 μm) diameter spherical microgels, respectively. We discovered that MAP scaffolds impart regenerative wound healing with an IgG1-biased Th2 response. MAP scaffolds made with large microgels promoted a balanced pro-regenerative macrophage response, resulting in enhanced wound healing with mature collagen regeneration and reduced inflammation levels.

Graphical Abstract

*Corresponding author: Prof. Tatiana Segura, tatiana.segura@duke.edu, Tel.: +1-919-660-2901.

Author contributions

YL made substantial contributions to the conceptualization and design of the work, acquisition, analysis, and interpretation of data, as well as writing the manuscript and addressing comments. ASA participated in the acquisition, analysis, and interpretation of data for both the subcutaneous and wound healing models, as well as drafting the manuscript and addressing comments. EC sectioned, stained, and performed histological quantification of wound samples found in figure 3 and Figure S2. LR computationally analyzed the scaffolds and provided analysis, interpretation, and writing. MS oversaw and performed histology assessment that contributed substantially to figure 3 and Figure S2. All the authors discussed the results and contributed to writing portions of the manuscript and editing the manuscript. TS conceptualized and conceived the project, provided guidance and discussion throughout, and made substantial contributions to data analysis, figure preparation, and manuscript editing.

Supporting Information

Supporting Information is available from the Wiley Online Library or from the author.

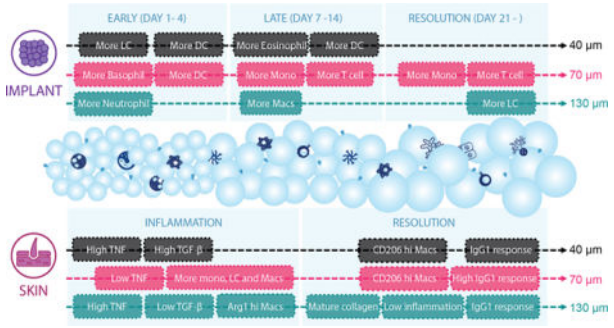

Keywords

spatial confinement; biomaterials; wound healing; macrophages; immune cells; foreign body response; granular materials

1. Introduction

When developing biomaterials for clinical use, their performance significantly depends on how they interact with the host immune system(Anderson, 1988; Anderson & McNally, 2011; Anderson & Miller, 1984). Failure to properly engage and incorporate the appropriate immune response may result in a foreign body response, leading to subsequent material rejection. This is due to a cascade of cellular responses(Anderson et al., 2008), including persistent inflammation, a build-up of foreign body giant cells, and fibrosis at the implant site. To optimize the biocompatibility of biomaterials and mitigate adverse immune responses, a wide range of design parameters were researched, such as surface modifications (e.g., a change in hydrophobicity or surface charge to reduce protein or cell absorption(Brodbeck et al., 2002; Jones et al., 2007), incorporating cell adhesive ligands to selectively engage immune cells(Cha et al., 2017; Lynn et al., 2010)) and stiffness(Blakney et al., 2012; Chen et al., 2020). Specifically, altering material porosity by varying the size of the void space inside biomaterial scaffolds has shown promise in mitigating immune response and promoting better tissue integration(Bota et al., 2010; Madden et al., 2010; Sussman et al., 2014). Having an interconnected network of void space inside the scaffold allows for easy traversal of cells and diffusion of biological factors(Dai et al., 2018), and it leaves room for the development of vasculature and stroma(Feng et al., 2011; Rosengren & Bjursten, 2003; Yin et al., 2020). The size and shape of the void space also apply spatial constraints onto the infiltrating cells, thereby modulating their behavior and phenotypes(Jain & Vogel, 2018).

Only a handful of studies examined the role of material porosity and spatial confinement (SC) on cellular behaviors and tissue regeneration *in vivo*. For example, researchers observed the most blood vessel formation with minimal fibrotic response in poly (2-hydroxyethyl methacrylate-co-methacrylic acid) (pHEMA) scaffolds with pore diameters of 30 or 40 μm following 2-week cardiac implantation in rats, compared to scaffolds with 20 μm pores or no pores(Madden et al., 2010). The existence of porous architectures in these scaffolds increased the macrophage mannose receptor (MMR, pro-regenerative

marker) level in nitric oxide synthase 2 (NOS2, pro-inflammatory marker) expressing macrophages(Madden et al., 2010). A similar study with the same pHEMA system uncovered that at 3 weeks post-implantation in mice, the pro-regenerative macrophage marker expression (MMR and scavenger receptor B I/II) was lower (<50%) inside 34 μm pores than in 160 μm pores(Sussman et al., 2014). Another work explored the influence of pore size-mediated macrophage polarization on angiogenesis(Yin et al., 2020). They reported that in a subcutaneous implantation model, collagen scaffolds with average pore sizes of 360 μm induced more vascularization and recruited more VEGF+ cells and fewer pro-inflammatory macrophages, compared to those with 160 μm pores. These findings contributed to the understanding that SC within scaffolds of different pore sizes can guide cellular infiltration and mitigate immune cell responses. Nevertheless, the conclusions did not consistently associate one specific pore size with a favorable immune response, nor did they cover a time course of the dynamic process of the material-cell interactions.

Granular scaffolds are an emerging platform for studying how SC impacts cellular behaviors and the host response to biomaterials(Caldwell et al., 2021; Liu, Suarez-Arnedo, Shetty, et al., 2022; Lowen et al., 2023; Riley et al., 2019). These materials are composed of microgel building blocks, which can be individually designed and collectively form constructs with desired mechanical and biochemical properties(Daly et al., 2020; Riley et al., 2019). The bottom-up design of granular materials offers many appealing characteristics, particularly injectable porosity. The particle size and subsequent pore size between particles are highly tunable, thereby enabling users to engineer SC within granular scaffolds(Caldwell et al.). In recent years, granular scaffolds have been leveraged in several applications as *in vitro* cell culture models as well as *in vivo* acellular and cell/molecule delivery therapeutics(Griffin et al., 2021; Hu et al., 2018; Rao et al., 2022; Veiseh et al., 2015). As this emerging platform gets widely utilized, understanding how SC within granular scaffolds modulates immune cell recruitment *in vivo* also empowers future designs to optimize particle size and induce specific cellular responses for target applications.

Microporous annealed particle (MAP) scaffolds are a type of granular material comprised of interlinked micron sized hydrogel particles (microgels) resulting in a void space network surrounding the microgels(D. R. Griffin et al., 2015). Initially designed to modulate the host response and improve cellular infiltration in wound healing(Donald R. Griffin et al., 2015), MAP scaffolds soon demonstrated potential in many applications (Caldwell et al., 2021; de Rutte et al., 2019; Hsu et al., 2019; Koh et al., 2019; Li et al., 2018; Pruett et al., 2020; Qazi et al., 2022; Seymour et al., 2021; Sheikhi et al., 2019; Suturin et al., 2022; Widener et al.; Xin et al., 2019; Xin et al., 2018). The modular nature of MAP scaffolds provides significant tunability, allowing for customization not only in individual microgel design but also in homogenous or heterogenous microgel assembly within the bulk scaffold(Qazi et al., 2022). When engineering MAP scaffolds, the size of the microgels composing MAP scaffolds dictates the internal landscape of the void space and the resulting SC that is sensed by cells(Liu, Suarez-Arnedo, et al., 2022b; Lowen et al., 2023; Riley, Cheng, et al., 2022) In this study, we explored the *in vivo* cellular response to MAP scaffolds with various particle sizes at different time points in a subcutaneous implant model and a wound healing model. We discovered that microgels of varying sizes with MAP scaffolds enable comparable levels of cell infiltration, which led to constructive innate and adaptive immune

responses. We employed a multifaceted flow cytometry phenotyping approach to quantify the infiltrating cell types and phenotypes in MAP scaffolds in both models. We concluded that the pore size-dependent recruitment and phenotype modulation of macrophages and other immune cells impacted the pro-healing effect observed in MAP scaffolds. Scaffolds comprised of large microgels with unconfined pore sizes resulted in a less inflammatory and more pro-regenerative responses.

2. Results and Discussion

2.1. 40 μm, 70 μm, and 130 μm MAP scaffolds were chemically and mechanically identical

Spherical microgels of different sizes were generated using different microfluidic devices with various run speeds (Figure 1a). The diameter of small microgels was around 40 μm, medium around 70 μm, and large 130 μm (Liu, Suarez-Arnedo, et al., 2022a). An analytical software (LOVAMAP) was developed in our lab to study and characterize different aspects of the void space inside MAP scaffolds for optimizing scaffold designs(Riley, Cheng, et al., 2022). This software segments the void space into natural pockets of open space (3D-pores) that are delineated at ‘doors,’ which are the narrower regions of void space between touching or nearby particles (Figure 1b). When the doors are on the surface of the scaffold, they are referred to as “entry doors” that infiltrating cells may use to enter the scaffold. We observed through confocal images that MAP scaffolds formed by different-sized microgels (abbreviated as 40 μm, 70 μm, 130 μm MAP scaffolds) had consistent void fraction (25–35%) but very distinct internal structures (Figure 1c)(Liu, Suarez-Arnedo, et al., 2022a). Using LOVAMAP to further characterize the interior of MAP scaffolds, we observed that the diameter range of the largest enclosed sphere within each 3D-pore in 40 μm MAP scaffolds mostly fell below the average size of a myeloid cell (Figure 1d). The same trend could also be observed for the diameter range of entry doors on the surface of 40 μm MAP scaffolds, whereas the diameters of most entry doors in 70 μm and 130 μm MAP scaffolds were larger than the diameter of a myeloid cell (Figure 1e). The microgel size-dependent shift in the pore and entry door profiles indicated that when these MAP scaffolds are used *in vivo*, they apply different degrees of spatial confinement on the infiltrating cells. We matched material stiffness for all three scaffold types so that the difference in cellular response could be attributed to the change in spatial confinement (a comprehensive characterization is detailed in a previous publication(Liu, Suarez-Arnedo, et al., 2022a)). It is crucial to note that the size of microgels not only affects the spatial confinement in the MAP scaffold but also the surface curvature that cells sense when inside the gel. Research has demonstrated that curvature can influence cell morphology and behavior, as it affects the shape of the cell membrane can trigger signaling cascades(Baptista et al., 2019; Callens et al., 2020; Orbach & Su, 2020). Nonetheless, because of the intricate shapes of the 3D void space inside the scaffold, the pore size is the measurable and distinct variable among the three MAP gels.

2.2 Immune cell recruitment and response followed a size-dependent manner in the subcutaneous implantation model

To explore the role of spatial confinement on immune cell recruitment in a non-traumatic setting, we characterized the infiltrating immune cell profile in a subcutaneous implantation

model. Each mouse received three injections of 50 μL hydrogel (one of each type, 40 μm, 70 μm, and 130 μm MAP scaffolds) on the back. After 1-, 4-, 7-, 14- and 21-days post-implantation, the infiltrated cells were extracted, and their phenotypes were analyzed by an 11-color innate immune cell panel (Figure 2a). This time window was chosen to explore the full spectrum of the foreign body response (FBR): days 1 and 4 correspond to the initial acute inflammatory phase, followed by a late inflammatory phase spanning around 7 to 14 days; the resolution phase occurs after 21 days. The total infiltrated live cell number and CD45+ cell number were similar among all MAP scaffolds groups (Figure 2b). This indicated that a smaller entry door size didn't pose a significant barrier to the cell infiltration, which can be due to the high shape plasticity of immune cells(Margraf & Perretti, 2022). Macrophages and FcεRI+ cells (such as Langerhan cells (LC), monocytes, mast cells, and other dendritic cells (DC)) dominated the immune cell infiltration(Liu, Suarez-Arnedo, et al., 2023) (Figure 2c). The immune cell recruitment followed a size-dependent manner. 130 μm MAP scaffolds recruited significantly more neutrophils within one day while 40 μm MAP scaffolds had elevated FcεRI+ cell percentage and 70 μm MAP scaffolds had a higher ratio of basophils (Figure 2d). Preceded by an elevation in infiltrating monocytes at day 4, the macrophage percentage peaked at day 7 in all the groups and most significantly in 130 μm MAP scaffolds (Figure 2d). Eosinophil level was increased at day 7 and more eosinophils were accumulated in 40 μm MAP scaffolds than 130 μm MAP scaffolds. As the FBR moved toward resolution, the percentage of FcεRI+ cells increased over time in all scaffolds and again was the highest in 130 μm MAP scaffolds (Figure 2d). The general immune response towards all MAP scaffolds was active but constructive, with an improved level of collagen deposition, granulation tissue, and vascularization 21-day post-implantation (Figure S1a).

2.3. 130 μm MAP scaffolds induced mature collagen regeneration and reduced inflammation in skin wounds.

To see how the size-dependent immune cell recruitment in MAP scaffolds would impact wound healing outcomes, we compared the effect of MAP scaffold treatment against a clinically used standard treatment Woun'Dres in a full-thickness excisional wound healing model in mice. To characterize the quality of tissue regeneration, we assessed the collagen architecture and maturity with Picro-Sirius red (PSR) staining and Masson's Trichrome (MT) staining (Figure 3a, Figure S2a, Figure S3a). In PSR, the amount of collagen and its architecture can be visualized and characterized by bright field and polarized light(Junqueira et al., 1979). In MT, the mature collagen appears in deep blue and has a basket weave-like network whereas newly regenerated collagen fibers are light blue in color and have more aligned fiber orientation(Gupta & Kumar, 2015; Xue & Jackson, 2015). Although all wounds had a higher collagen/fibroblast score (Figure S2), as our excisional splinted wound healing model in mice is designed to replicate re-epithelization and granulation tissue formation(Masson-Meyers et al., 2020), we do not anticipate the presence of human hypertrophic scarring or keloids, which are characterized by thick and excessive collagen bundles (Marshall et al., 2018). Instead, we define scar tissue in this model as the area lacking secondary appendages present in normal skin and regions of connective tissues devoid of the basket weave motif of collagen fibers observed in unwounded skin. 130 μm MAP scaffolds treated wounds appeared to have a structure more closely resembling normal

skin around the wound bed, showing better collagen regeneration with a higher collagen percentage and longer average fiber length than Woun'Dres group (Figure 3a–c). The 130 μm MAP scaffold group had the highest average epidermis to dermis (E/D) ratio, which was statistically greater than the rest of the groups and closer to the normal skin baseline (Figure 3e). Both 40 μm and 130 μm MAP scaffold groups had a lower afollicular percentage (greatest distance between two follicular structures in the wound bed divided by the total length of the wound) than Woun'Dres group (Figure 3f), indicating a smaller "true scar" region within the wounds.

Improved regeneration of the skin was also supported by the timely resolution of inflammation and matrix remodeling. CD11b+ immune cell accumulation, an indication of the general inflammation level, in the connective tissue of MAP scaffolds-treated wounds was close to that of normal skin, whereas the Woun'Dres group still had a significantly higher level than the baseline (Figure 3d, g). In the remaining biomaterials in the wound bed, 130 μm MAP scaffolds and Woun'Dres treatment both had a CD11b+ cell amount not significantly different than the basal level (Figure 3d, h). A similar trend was also confirmed by the histological assessment that the general inflammation level on day 21 was lower in 130 μm MAP scaffolds when compared to Woun'Dres groups (Figure S2b). Myofibroblasts, a major cell type secreting extracellular matrix (ECM), are responsible for depositing and replacing collagen during wound healing and fibrosis(Hinz & Lagares, 2020). An excess of myofibroblasts, characterized by the expression of alpha-smooth muscle actin (α-SMA), at the resolution phase of wound healing is associated with fibrosis(Klingberg et al.). In the newly formed connective tissue, MAP scaffolds groups restored the α-SMA+ myofibroblast level to the baseline while Woun'Dres group remained at a significantly higher level of α-SMA+ cell accumulation (Figure 3d, i). Within the remaining biomaterials, only the 130 μm MAP scaffolds group had a α-SMA+ cell level close to that in normal skin (Figure 3d, j), suggesting a better resolution of matrix remodeling.

ELISA results reviewed a size-specific cytokine profile at day 21. Notably, TGF-β, a cytokine associated with tissue regeneration and fibrosis(Abarca-Buis et al., 2021; Frangogiannis, 2020), was significantly increased in 40 μm MAP scaffolds treated wounds compared to 130 μm MAP scaffolds treated wounds, which pointed to a resolution of remodeling in 130 μm MAP scaffolds group after 21 days (Figure 3k). TNF, a potent inflammatory cytokine, was elevated significantly both in 40 μm and 130 μm MAP scaffold groups (Figure 3l). IL-1β, a macrophage activation cytokine, was generally expressed in all the treatment groups (Figure S2m). The key cytokine for Th2 immune response IL-4 was only expressed at a relatively low level in all groups (Figure S2n). Collectively, these results indicated a refined skin regeneration was promoted in wounds treated by a less confined scaffolds.

2.4. Immune cell recruitment followed a size-dependent manner in skin wounds

An effective and efficient wound repair requires the coordination of many different cell types, especially the immune cells during the inflammation phase. Given the improved wound healing outcomes we observed in MAP scaffold-treated wounds, especially with 130 μm MAP scaffolds, we further explored the immune cell profile in the skin wounds. We

sampled a 5 mm area around the initial wound site at days 1, 7, and 21. We selected this time window to investigate the acute immune response towards the materials on days 1 and 7, as well as the resolution phase at 21 days post-wounding (Figure 4a). The total infiltrated live cell number and CD45+ cell number were similar among all groups, again confirming that the size range of the entry door in MAP scaffolds was still large enough to allow sufficient cell infiltration (Figure 4b). To gain an overview of cellular infiltration, a representative profile was mapped out for all treatment groups (Figure 4c). Neutrophils and monocytes dominated the immune cell infiltration at day 1. 40 μm and 130 μm MAP scaffolds recruited more neutrophils than 70 μm MAP scaffolds whereas 70 μm MAP scaffolds attracted the highest percentages of monocytes, macrophages, and FcεRI+ cells (Figure 4d), which are the main immune modulators and antigen presenting cells (APCs) in the skin wound. At day 7, neutrophils and basophils took up most of the immune cells while T cells and basophils were the major cell types in the immune infiltrate 21-day post-wounding (Figure 4c). Since we observed size-dependent immune cell recruitment (Figure 4d), specifically at day 1, we sought to explore further the impact of spatial confinement on immune cell phenotype and focus on macrophages, a key immune modulator during wound healing.

2.5. 130 μm MAP scaffolds modulated a timely transition in pro-regenerative macrophage phenotypes

Spatial confinement of macrophages, an essential cell type in wound healing, has been shown to result in a less inflammatory phenotype(Jain & Vogel, 2018). We explored the change in macrophage phenotype during the wound healing process and in response to the change in spatial confinement. A significantly higher number of macrophages infiltrated 40 μm MAP scaffolds and Woun'Dres groups than 70 μm and 130 μm MAP scaffolds groups at day 1 (Figure 5a). Around 60% of these macrophages expressed Ly6C, which indicated an origin from circulating monocytes in blood (Figure 5b). The Ly6C+ macrophage percentage dropped in MAP scaffolds groups at day 7 as the cells differentiated into macrophages and assumed specific functions (Figure 5b). Almost all the macrophages were fully mature and lost Ly6C expression after 21 days (Figure 5b).

Macrophages in all the wounds showed a time-dependent phenotype transition (Figure 5c). Higher levels of pro-inflammatory/co-stimulatory marker CD86 and antigen-presenting marker CD11c were observed at day 1. Antigen-presenting marker MHCII was also highly expressed at days 1 and 7. The expression of these markers suggested the active antigen presentation role macrophages play during the early wound healing response. Nitric oxide (NO) release has been previously reported to significantly reduce collagen encapsulation and chronic inflammation in foreign body response(Nichols et al., 2012). The pro-inflammatory marker inducible nitric oxide synthase (iNOS), a key enzyme driving the production of immunomodulating molecule NO, remained highly expressed at days 7 and 21 as the wound moved towards resolution. Notably, both pro-regenerative markers Arginase 1 (Arg1) and CD206 demonstrated size-dependent shifts in expression. The induction of arginase activity in the wound could cause the depletion of arginine, which provides substrates indirectly contributing to collagen deposition(Szondi et al., 2021). Arg1 was highly expressed in wound macrophages at day 1, especially in the 130 μm MAP scaffolds group. CD206 levels were also elevated in all MAP scaffolds groups, 40 μm and 70 μm MAP scaffolds

in particular, at day 21. A significantly lower level of CD206 as day 21 in 130 μm MAP scaffolds wounds compared to 40 μm and 70 μm MAP scaffolds groups, together with a generally tamed expression of the other five functional markers. This pointed to a resolution of macrophage response in 130 μm MAP scaffolds that might in part contribute to the better wound resolution and more mature collagen regeneration.

To further characterize the macrophage phenotype profile at day 1 (the initial acute immune response with the most macrophage accumulation), we used FlowSOM, an unsupervised algorithm based on Self-Organizing Maps, to reveal how all six functional markers were behaving on macrophages and distinguish distinct subpopulations(Quintelier et al., 2021). The differentiation of these macrophage populations was determined by analyzing the expression levels of each marker (shown in the table below the histogram plot, "+" meant over 50% population expressed that marker). FlowSOM analysis revealed that MAP scaffolds attracted similar macrophage profiles, effectively polarizing them into a diverse array of phenotypes. Remarkably, in certain cases (population 2, 4, 6), the pro-inflammatory markers CD86 and/or iNOS were co-expressed with the pro-regenerative markers CD206 and/or Arginase 1. This finding supported that macrophage phenotypes exist on a spectrum and their functions cannot be fully captured by one or two markers. Seven distinct macrophage populations were identified. Population 1, which expressed CD86 and MHCII, was an antigen-presenting phenotype and the major macrophage subpopulation in all wounds. 130 μm MAP scaffolds-treated wounds recruited higher percentages of population 2 (Arg1+CD86+MHCII+, M2-biased antigen-presenting phenotype) and 4 (Arg1+CD86+CD206+, M2-biased hybrid phenotype), both expressing a high level of Arg1 and exhibiting a pro-regenerative polarization. Collectively, these observations confirmed that MAP scaffolds induced a complex macrophage response with unique expression profiles. 130 μm MAP scaffolds promoted an early pro-regenerative macrophage profile and modulated a timely resolution in macrophage response towards the end of the wound healing process.

2.6. A pro-reparative IgG1-biased Th2 response was observed in 70 μm MAP scaffolds

Since a significant amount of adaptive immune cells, especially T cells, were recruited to the wounds after material treatment, we examined whether the application of MAP scaffolds would lead to any systemic adaptive immune response. Notably, by day 21, all mice subjected to MAP scaffold treatment demonstrated the development of a specific IgG response against the MMP linker, with 70 μm MAP scaffolds having the most drastic increase compared to the untreated control (Figure 6a). This MAP scaffolds-induced response was IgG1-biased and therefore a pro-reparative Th2 response (Figure 6b). We also investigated the adaptive immune cell profiles of draining lymph nodes (dLN) and the spleen in MAP scaffolds-treated mice 1-day, 7-day, and 21-day post-wounding. MAP scaffolds treatment also modulated T cell profile and an increase in Th2 marker GATA3 expression in dLN at day 7 and in the spleen at days 7 and 21 was observed (Figure 6c,d). Compared to the baseline, the Th1 marker Tbet level was significantly reduced in dLN at days 7 and 21 and in almost all groups except 70 μm MAP scaffolds at day 7 in the spleen (Figure 6c,d). The evidence provided here demonstrates that a pro-regenerative Th2 adaptive immune response can be engaged by synthetic pro-regenerative scaffolds and

its magnitude was modulated by the size of the microgels(Griffin et al., 2021) (Figure 6c,d, Figure S3). Our findings suggested that different microgel sizes of MAP scaffolds have positive effects on wound resolution and regeneration, despite unique immune profiles for both subcutaneous and wound healing models (Figure 6e,f). 130 μm MAP leverage a pro-healing response associated with early pro-regenerative macrophage profiles, mature collagen deposition, and low inflammation during wound resolution. These findings align with previous studies demonstrating that granular materials with a pore size between 30μm and 40μm diameter spheres can induce a regenerative response and reduce the foreign body reaction (FBR) (Chan et al., 2022; Hady et al., 2023). It is important to note that the observed differences between the main temporal changes at the implant and wound site cannot solely be attributed to the context-dependent environment, but also to the different mice strains used in the experiments. The SKH1 and B6 mice strains differ in genetic and phenotypic characteristics. For instance, SKH1 mice used in the wound healing model exhibit a higher humoral response, while the immune response of B6 mice tends to be Th1-biased(Li et al., 2021; Schaffer et al., 2010).

3. Discussion

Pore size has long been a key design parameter for biomaterials. As the entry points into scaffolds, the pore size on the surface of materials poses limitations for infiltrating cells and ingrowing tissues. A small pore size, usually on the nanoscale or below 10 microns, is known to prevent cellular infiltration and is more prone to induce a foreign body response(Rosengren & Bjursten, 2003; Sussman et al., 2014). On the other hand, larger pore sizes of tens to hundreds of microns could be beneficial for nutrient transport and the growth of connective tissue and blood vessels(Sussman et al., 2014; Wang et al., 2014; Yin et al., 2020), which supports implant success rate in the long run. Once the infiltrating cells are in the interior of the scaffolds, the size and architecture of the void space influences cell morphology, phenotype, and activity by imposing spatial constraint and confinement. Spatially confining immune cells, such as macrophages, can modulate their phenotype and their inflammatory response(Jain & Vogel, 2018). Scaffolds with an optimized pore size should support the initial influx of immune cells and offer sufficient spatial confinement to modulate cell phenotype while accommodating structural regeneration.

In this study, we demonstrated that microporous annealed particle scaffolds (MAP scaffolds) consisting of different-sized microgels (40 μm, 70 μm, and 130 μm diameter) imparted regenerative wound healing with an IgG1-biased Th2 response when compared to clinical standard treatment. 130 μm MAP scaffolds with a pore size that can accommodate ~40 μm diameter spheres induced mature collagen regeneration and reduced levels of inflammation in the skin wound. Pore size-dependent recruitment and phenotype modulation of macrophages and other immune cells impacted the pro-healing effect observed in MAP scaffolds. These findings suggest that pore size can be specifically engineered to modulate the functions of infiltrating cells and trigger regeneration rather than fibrosis. Future directions combining the MAP scaffolds platform with other immune or pro-regenerative factors can further leverage its potent immunomodulatory potential for optimal skin regeneration.

4. Experimental section/Methods

Microparticle generation and purification:

Microfluidic devices and microgels were made as previously described(Liu, Suarez-Arnedo, et al., 2023). Briefly, 8 arm PEG-VS microgels were formulated at a final concentration of 5 wt% (w/v) PEG-VS (JenKem technology) in 0.3 M triethanolamine (Sigma) with 500 μM RGD (Ac-RGDSPGERCG-NH2, GenScript), 500 μM K-peptide (Ac-FKGGERCG-NH2, GenScript) and 500 μM Q-peptide (Ac-NQEQVSPLGGERCG-NH2, GenScript) and crosslinked at a 0.6 VS to thiol ratio with di-thiol matrix metalloproteinase sensitive peptide (Ac-GCRDGPQGIWGQDRCG-NH2,GenScript) plus 10 μM AlexaFluor-647 (ThermoFisher). For 40 μm and 70 μm microgel generation, we used a four-inlet microfluidic device. For 130 μm microgel generation, we used a two-inlet microfluidic device.

Generation of MAP scaffolds from microgels and mechanical testing:

The storage buffer in microgels was properly removed by centrifuging at 22 000 G for 5–20 minutes and taking off the supernatant. For every 50 μL of dried microgels, 2 μL of Factor XIII (250 U/mL) and 1 μL of Thrombin (200 U/mL in 200 mM Tris-HCl, 150 mM NaCl, 20 mM CaCl2) was added and mixed via thorough pipetting. A 30-minute incubation time at 37°C is required to form a bulk hydrogel scaffold. Rotational rheometry (Anton-Parr, MCR301) was used to measure the storage moduli of the scaffolds with a frequency sweep test (0.1–100 rad/s shear frequency and 1% strain amplitude).

Microgel size and void volume measurement:

Microgel size was calculated using a custom MATLAB code(Riley, Wei, et al., 2022) from at least three 4X images (Nikon Ti Eclipse) per batch of microgels and an average of at least five batches of microgels. For scaffold void volume measurement, three scaffolds were sampled for each type of scaffold (40 μm, 70 μm and 130 μm MAP scaffolds). Three regions of interest were randomly selected inside each scaffold and a 140 μm thick z-stack sample (509 z-slices, 0.275 um each step) was taken in each ROI at an objective of 40X. IMARIS (Oxford instruments) was used to analyze the images for void volume fraction calculation.

Subcutaneous implantation:

7–12-week-old male C57BL/6 mice were purchased from Jackson Laboratory. The microgels and crosslinker solution were thoroughly mixed and loaded in a 1 cc insulin syringe with a 29-gauge needle. Each mouse received three injections of 50 μL hydrogel (one of each, 40 μm, 70 μm, and 130 μm MAP scaffolds) on the back. All procedures were approved by the Duke University Institutional Animal Care and Use Committee under protocol A085-21-04 (Principal investigator: Tatiana Segura) and followed the NIH Guide for the Care and Use of Laboratory Animals.

Implant extraction and flow cytometry study:

At selected time points, the implants were extracted and cell extraction was performed as previously described(Liu, Suarez-Arnedo, et al., 2023). An enzymatic digestion with the

digestion solution (200 U/ml Collagenase IV and 125U/ml DNase I) in RPMI media was used. Samples were stained and prepared following manufacturer instructions, and analyzed on the Cytek NL-3000 Flow Cytometer. Data was acquired using SpectroFlo software and analyzed using FlowJo™ v10.8 Software (BD Life Sciences).

Flow cytometry data clustering was performed by pooling an equal number of cells from all biological replicates into a single file and using the tSNE (t-distributed stochastic neighbor embedding) plugin with 1000 iterations, theta = 0.5. The results were displayed as user-gated populations graphed against their respective X and Y tSNE coordinates. Further clustering was conducted with the FlowSOM algorithm on the concatenated files, and the main immune subsets were phenotypically isolated through the selection of 5–8 metaclusters. Each subset was then characterized based on the expression or absence of different phenotypical markers.

Wound healing study:

10–12 weeks old female and male SKH-1 Elite mice were purchased from Charles River. The excisional splinted wound protocol used in this study is a well-established methodology previously reported by others(Galiano et al., 2004) and is described in detail in our earlier publication(Zhu et al., 2018). Briefly, mice were anesthetized with 4% isoflurane and maintained at 1.5–2% isoflurane throughout the surgery. To prevent additional pain and hypothermia, mice were placed on a warming pad and Buprenorphine SR-Lab (ZooPharma) was injected subcutaneously at 0.5 μg per gram of mouse weight. The dorsal surface was sterilized with iodine and ethanol three times each. Using sterile 5 mm biopsy punches (Integra Miltex), four clean and well-defined wounds were generated along the middle of the animal's back. To facilitate wound healing through re-epithelialization and granulation tissue deposition, aseptic sticky PDMS silicon ring splints with a 7-mm wide window were carefully applied to the wounds(Galiano et al., 2004). Following this, a mixture of microgels and annealing solution was promptly administered to the wounds. After 30-minute gelation time, animals were carefully wrapped with Tegaderm dressings (3M, Inc.) and monitored until full recovery from the anesthesia. Animals were housed individually in cages with sufficient enrichments, weighted for the first seven days post-operation, and checked on every other day afterward.

ELISA:

Mouse serum was collected at designated time points and analyzed for antibody titers by ELISA, as previously described(Hartman et al., 2018; Liu, Suarez-Arnedo, et al., 2023). Briefly, plates were coated overnight at 4℃ with MMP peptide solution (20 μg /ml) or PBS, then washed with 1XPBS + 0.5% Tween 20 (PBST) and blocked with Superblock (ThermoFisher). In a separate plate, serum was serially diluted fourfold in 1%BSA in PBST starting at a 1:100 dilution and ending at a 1:100000 dilution. Serum :)dilutions were added to the antigen-coated plates to peptide-coated and PBS wells, and incubated for 2 h, followed by washes with PBST. HRP-conjugated Fcγ fragment-specific goat anti-mouse IgG (Jackson Immunoresearch) was diluted to 1:5000, added to the plates and incubated at room temperature for 45 min. These plates were washed and developed with TMB substrate (ThermoFisher). For antibody isotyping, HRP-conjugated IgG subtype-specific antibodies

(IgG1, IgG2b, IgG2c, and IgG3) from Southern Biotech were used instead of the total IgG detection antibody. The reaction was stopped after 5 min with 1 M HCl, and OD at 450 nm was measured using a Spectramax i3X microplate reader (Softmax Pro 3.1 software; Molecular Devices). Titers were calculated as area under the transformed curve (AUC) using GraphPad Prism after subtracting the background PBS well OD values from the peptide-coated well OD values. The y-axis values correspond to the log of the serum dilution 2, 3, 4 and 5 respectively i.e. OD values at higher dilutions correspond with higher titers.

Histology staining:

At specified time points, implants or wound samples were collected for histology examination. For paraffin embedding, the samples were fixed with 4% paraformaldehyde overnight at 4°C and then underwent further processing. Paraffin blocks were sectioned into 5 μm thickness, with a minimum of 3 serial-sections per slide for hematoxylin and eosin (H&E) staining, masson trichrome staining, Picro-Sirius red staining, and immunohistochemistry (IHC) staining.

For H&E staining, paraffin-embedded sections were de-waxed and hydrated using xylene then decreasing ethanol concentrations. They were stained in Mayer Hematoxylin Solution (EMS) for 15 minutes before being rinsed in warm running tap water for 15 minutes. They were placed in DI water for 30 seconds, 95% ethanol for 30 seconds, and then into Alcoholic Eosin Y Counterstain (EMS) for 30 seconds. They were then dehydrated and cleared before being mounted in DPX (EMS).

For Masson's Trichrome staining, paraffin-embedded sections were de-waxed and hydrated using xylene then decreasing ethanol concentrations. They were mordanted in Bouin's Fixative (EMS) overnight at room temperature. The slides were rinsed in DI water for 15 minutes. They were then stained in Weigert's Iron Hematoxylin Working Solution (EMS) for 5 minutes and rinsed in DI water for 10 minutes. The slides were placed in Biebrich Scarlet-Acid Fuchsin (EMS) for 15 minutes and rinsed in DI water for 5 minutes. Next, they were stained in Phosphomolybdic Acid-Phosphotungstic Acid (EMS) for 15 minutes and then in Aniline Blue (EMS) for 10 minutes. The slides were washed in DI water for 5 minutes and differentiated in 1% (v/v) Acetic Acid. They were then dehydrated and cleared before being mounted in DPX (EMS).

For Picro-Sirius red staining, paraffin-embedded sections were de-waxed and hydrated using xylene then decreasing ethanol concentrations. The sections were then stained in Picro-Sirius red (Spectrum Chemical) for one hour. They were then washed two tines in acidified water for 2 minutes each. They were then dehydrated and cleared before being mounted in DPX (EMS)(Junqueira et al., 1979).

For IHC staining, the paraffin-embedded slides were deparaffinized using xylene and descending ethanol. Antigen retrieval was performed by incubating the slides in 10 mM sodium citrate buffer with 0.05% Tween 20 (pH 6) at 95°C using a microwave for 20 minutes. The slides were allowed to cool to room temperature and then rinsed in PBST (Phosphate Buffered Saline containing 0.05% Tween-20). Subsequently, the slides were stained with rabbit primary antibodies (anti-mouse CD11b antibody from Novus Biologicals

or anti-mouse α-SMA antibody from Abcam) and incubated at 4°C overnight. To visualize CD11b or α-SMA in brown, the ImmPRESS® Horse Anti-Rabbit IgG PLUS Polymer Kit from Vector Laboratories was used. After washing in tap water, the slides were counterstained with Mayer hematoxylin solution (EMS), dehydrated in ethanol, and finally mounted with DPX (EMS).

In vivo quantification and analysis:

All stained slides were subjected to full section scans using ZEISS Axio Scan.Z1. Image quantification was performed using an in-house algorithm in ImageJ to determine the CD11b+ and α-SMA+ cell areas as ratios of the nucleus area. Briefly, three regions of interest were manually drawn in the connective tissue, inside the remaining biomaterials, and in normal skin. The total nucleus area was calculated after color deconvolution with the H&E DAB vector module and thresholding in the blue channel using the 'Max Entropy' method. In the brown channel, another thresholding method ('IsoData') was applied to quantify the positive areas of CD11b or α-SMA. The expression of each marker was normalized by dividing the positive marker area by the total nucleus area. The remaining MAP scaffolds percentage in the wound was calculated by selecting manually and measuring the area of MAP scaffolds as well as the wound. The epidermis to dermis ratio was measured using an in-house algorithm in ImageJ. Briefly, the dermis area and epidermis area were manually selected using the Freehand Selection tool. The areas were saved and analyzed using a code that measures the width of the epidermis and dermis at multiple matching intervals along the selection. These values were used to create multiple epidermis to dermis ratios and produce a histogram of values with a count, average, and standard deviation. Collagen alignment was measured using were selecting five regions of 100 μm^2 and the anisotropy was quantified using Fibriltool(Boudaoud et al., 2014). Area of collagen, average collagen length and average collagen width were measured on brightfield images of Picro-Sirius red. These images were thresholding with "IsoData" method, and the masks were used to quantified collagen architecture features.

H&E sections were independently examined by a board-certified dermatopathologist (P.O.S.), who remained blinded to the identity of the samples. The assessment involved various aspects of wound healing, including re-epithelialization, granulation tissue formation, vascularization, collagen deposition, fibrosis/fibroplasia (early scar formation), and inflammation. A modified 12-point scoring system was used for evaluation, which had been established and agreed upon by two dermatopathologists (details listed in Tables S1–S5)(Cam et al., 2015). Within all MAP scaffolds-treated wounds, we also quantified key markers including the number of hair follicle structures, the number of sebaceous glands, and the number of dermal cysts. Hair follicle-like structures were grouped with utricular pouches, a common structure in SKH-1 mouse skin raised from the infundibulum of the hair shaft (the upper portion of the follicle)(Benavides et al.). Only the structural features within the inner 60% of the wound were quantified to ensure the regions of interest were within the wound bed and not related to the primary intention of the skin surrounding the injury.

Statistics and reproducibility:

All statistical analyses were performed using Prism 9 software (GraphPad, Inc.). One-way or two-way ANOVA was utilized to determine statistical significance. For one-way ANOVA, a post hoc analysis with Dunnett's multiple comparisons test was conducted, while for two-way ANOVA, multiple comparisons were performed using Šídák's multiple comparisons test. The subcutaneous implantation studies were replicated three times (n=5, all-male) and examined with an 11-color innate flow cytometry panel or a 7-color macrophage panel (representative results Figure S7). The wound healing study was repeated twice (n=5, mixed-gender) and evaluated using a 13-color innate flow cytometry panel and/or histological analysis.

Supplementary Material

Refer to Web version on PubMed Central for supplementary material.

Acknowledgements

We would like to thank the National Institutes of Health (R01AI152568) and all the members of the Segura lab at Duke University for their support. A special thank you to Shamitha Shetty and Christopher Lloyd at Duke University for their generous help and delightful company. Thank you to April Espinoza for helping with part of the experiment. Thank you to our lab alumni Jingyi Xia for assistance in material characterization. Thank you to Patrick Duncker, Ph.D. at Cytek Biosciences for providing technical support on spectral flow cytometry and sharing insights on data interpretation. Thank you to Minerva Matos-Garner, MA from Duke Engineering Graduate Communications and Intercultural Programs for her constructive suggestions on the manuscript and her warm support during the writing process. This work was performed in part at the Duke University Light Microscopy Core Facility (LMCF) and with help from Yasheng Gao, PhD.

Data availability

The data that support the findings of this study are available from the corresponding authors upon reasonable request. Source data are provided with this paper.

References

Abarca-Buis RF, Mandujano-Tinoco EA, Cabrera-Wrooman A, & Krötzsch E (2021). The complexity of TGFβ/activin signaling in regeneration. Journal of Cell Communication and Signaling, 15, 7–23. [PubMed: 33481173]

Anderson JM (1988). Inflammatory response to implants. ASAIO Trans, 34(2), 101–107. 10.1097/00002480-198804000-00005 [PubMed: 3285869]

Anderson JM, & McNally AK (2011). Biocompatibility of implants: lymphocyte/macrophage interactions. Seminars in Immunopathology, 33(3), 221–233. 10.1007/s00281-011-0244-1 [PubMed: 21271251]

Anderson JM, & Miller KM (1984). Biomaterial biocompatibility and the macrophage. Biomaterials, 5(1), 5–10. 10.1016/0142-9612(84)90060-7 [PubMed: 6375747]

Anderson JM, Rodriguez A, & Chang DT (2008). Foreign body reaction to biomaterials. Seminars in Immunology, 20(2), 86–100. 10.1016/j.smim.2007.11.004 [PubMed: 18162407]

Baptista D, Teixeira L, van Blitterswijk C, Giselbrecht S, & Truckenmüller R (2019). Overlooked? Underestimated? Effects of substrate curvature on cell behavior. Trends in biotechnology, 37(8), 838–854. [PubMed: 30885388]

Benavides F, Oberyszyn Tm Fau - VanBuskirk AM, VanBuskirk Am Fau - Reeve VE, Reeve Ve Fau - Kusewitt DF, & Kusewitt DF The hairless mouse in skin research. (0923–1811 (Print)).

Blakney AK, Swartzlander MD, & Bryant SJ (2012). The effects of substrate stiffness on the in vitro activation of macrophages and in vivo host response to poly(ethylene glycol)-based hydrogels. J Biomed Mater Res A, 100(6), 1375–1386. 10.1002/jbm.a.34104 [PubMed: 22407522]

Bota PC, Collie AM, Puolakkainen P, Vernon RB, Sage EH, Ratner BD, & Stayton PS (2010). Biomaterial topography alters healing in vivo and monocyte/macrophage activation in vitro. J Biomed Mater Res A, 95(2), 649–657. 10.1002/jbm.a.32893 [PubMed: 20725970]

Boudaoud A, Burian A, Borowska-Wykręt D, Uyttewaal M, Wrzalik R, Kwiatkowska D, & Hamant O (2014). FibrilTool, an ImageJ plug-in to quantify fibrillar structures in raw microscopy images. Nature protocols, 9(2), 457–463. [PubMed: 24481272]

Brodbeck WG, Patel J, Voskerician G, Christenson E, Shive MS, Nakayama Y, Matsuda T, Ziats NP, & Anderson JM (2002). Biomaterial adherent macrophage apoptosis is increased by hydrophilic and anionic substrates in vivo. Proc Natl Acad Sci U S A, 99(16), 10287–10292. 10.1073/pnas.162124199 [PubMed: 12122211]

Caldwell AS, Campbell GT, Shekiro KMT, & Anseth KS Clickable Microgel Scaffolds as Platforms for 3D Cell Encapsulation. LID - 10.1002/adhm.201700254 [doi]. (2192–2659 (Electronic)).

Caldwell AS, Rao VV, Golden AC, Bell DJ, Grim JC, & Anseth KS (2021). Mesenchymal stem cell-inspired microgel scaffolds to control macrophage polarization. Bioengineering & Translational Medicine, 6(2), e10217. [PubMed: 34027099]

Callens SJP, Uyttendaele RJC, Fratila-Apachitei LE, & Zadpoor AA (2020). Substrate curvature as a cue to guide spatiotemporal cell and tissue organization. Biomaterials, 232, 119739. [PubMed: 31911284]

Cam C, Zhu S, Truong NF, Scumpia PO, & Segura T (2015). Systematic evaluation of natural scaffolds in cutaneous wound healing. Journal of materials chemistry. B, 3(40), 7986–7992. 10.1039/C5TB00807G [PubMed: 26509037]

Cha B-H, Shin SR, Leijten J, Li Y-C, Singh S, Liu JC, Annabi N, Abdi R, Dokmeci MR, Vrana NE, Ghaemmaghami AM, & Khademhosseini A (2017). Integrin-Mediated Interactions Control Macrophage Polarization in 3D Hydrogels. Advanced Healthcare Materials, 6(21), 1700289. 10.1002/adhm.201700289

Chan NR, Hwang B, Ratner BD, & Bryers JD (2022). Monocytes contribute to a pro-healing response in 40 μm diameter uniform-pore, precision-templated scaffolds. Journal of tissue engineering and regenerative medicine, 16(3), 297–310. [PubMed: 34964563]

Chen M, Zhang Y, Zhou P, Liu X, Zhao H, Zhou X, Gu Q, Li B, Zhu X, & Shi Q (2020). Substrate stiffness modulates bone marrow-derived macrophage polarization through NF-kappaB signaling pathway. Bioact Mater, 5(4), 880–890. 10.1016/j.bioactmat.2020.05.004 [PubMed: 32637751]

Dai Y, Li X, Wu R, Jin Y, & Gao C (2018). Macrophages of Different Phenotypes Influence the Migration of BMSCs in PLGA Scaffolds with Different Pore Size [https://doi.org/10.1002/biot.201700297]. Biotechnology Journal, 13(1), 1700297. https://doi.org/10.1002/biot.201700297

Daly AC, Riley L, Segura T, & Burdick JA (2020). Hydrogel microparticles for biomedical applications. Nature Reviews Materials, 5(1), 20–43. 10.1038/s41578-019-0148-6

de Rutte JM, Koh J, & Di Carlo D (2019). Scalable high-throughput production of modular microgels for in situ assembly of microporous tissue scaffolds. Advanced Functional Materials, 29(25), 1900071.

Feng B, Jinkang Z, Zhen W, Jianxi L, Jiang C, Jian L, Guolin M, & Xin D (2011). The effect of pore size on tissue ingrowth and neovascularization in porous bioceramics of controlled architecture in vivo. Biomed Mater, 6(1), 015007. 10.1088/1748-6041/6/1/015007 [PubMed: 21206002]

Frangogiannis NG (2020). Transforming growth factor–β in tissue fibrosis. Journal of Experimental Medicine, 217(3).

Galiano RD, Michaels J. t., Dobryansky M, Levine JP, & Gurtner GC (2004). Quantitative and reproducible murine model of excisional wound healing. Wound Repair Regen, 12(4), 485–492. 10.1111/j.1067-1927.2004.12404.x [PubMed: 15260814]

Griffin DR, Archang MM, Kuan C-H, Weaver WM, Weinstein JS, Feng AC, Ruccia A, Sideris E, Ragkousis V, Koh J, Plikus MV, Di Carlo D, Segura T, & Scumpia PO (2021). Activating an adaptive immune response from a hydrogel scaffold imparts regenerative wound healing. Nature Materials, 20(4), 560–569. 10.1038/s41563-020-00844-w [PubMed: 33168979]

Griffin DR, Weaver WM, Scumpia PO, Di Carlo D, & Segura T (2015). Accelerated wound healing by injectable microporous gel scaffolds assembled from annealed building blocks. Nature Materials, 14(7), 737–744. 10.1038/nmat4294 [PubMed: 26030305]

Gupta A, & Kumar P (2015). Assessment of the histological state of the healing wound. Plastic and Aesthetic Research, 2, 239–242. 10.4103/2347-9264.158862

Hady TF, Hwang B, Waworuntu RL, Ratner BD, & Bryers JD (2023). Cells resident to precision templated 40-μm pore scaffolds generate small extracellular vesicles that affect CD4+ T cell phenotypes through regulatory TLR4 signaling. Acta biomaterialia.

Hartman H, Wang Y, Schroeder HW Jr, & Cui X (2018). Absorbance summation: A novel approach for analyzing high-throughput ELISA data in the absence of a standard. PloS one, 13(6), e0198528. [PubMed: 29883460]

Hinz B, & Lagares D (2020). Evasion of apoptosis by myofibroblasts: a hallmark of fibrotic diseases. Nature Reviews Rheumatology, 16(1), 11–31. 10.1038/s41584-019-0324-5 [PubMed: 31792399]

Hsu RS, Chen PY, Fang JH, Chen YY, Chang CW, Lu YJ, & Hu SH (2019). Adaptable microporous hydrogels of propagating NGF-gradient by injectable building blocks for accelerated axonal outgrowth. Advanced Science, 6(16), 1900520.

Hu Z, Ma C, Rong X, Zou S, & Liu X (2018). Immunomodulatory ECM-like Microspheres for Accelerated Bone Regeneration in Diabetes Mellitus. ACS Applied Materials & Interfaces, 10(3), 2377–2390. 10.1021/acsami.7b18458 [PubMed: 29280610]

Jain N, & Vogel V (2018). Spatial confinement downsizes the inflammatory response of macrophages. Nat Mater, 17(12), 1134–1144. 10.1038/s41563-018-0190-6 [PubMed: 30349032]

Jones JA, Chang DT, Meyerson H, Colton E, Kwon IK, Matsuda T, & Anderson JM (2007). Proteomic analysis and quantification of cytokines and chemokines from biomaterial surface-adherent macrophages and foreign body giant cells. J Biomed Mater Res A, 83(3), 585–596. 10.1002/jbm.a.31221 [PubMed: 17503526]

Junqueira LCU, Bignolas G, & Brentani RR (1979). Picrosirius staining plus polarization microscopy, a specific method for collagen detection in tissue sections. The Histochemical journal, 11, 447–455. [PubMed: 91593]

Klingberg F, Hinz B Fau - White ES, & White ES The myofibroblast matrix: implications for tissue repair and fibrosis. (1096–9896 (Electronic)).

Koh J, Griffin DR, Archang MM, Feng A-C, Horn T, Margolis M, Zalazar D, Segura T, Scumpia PO, & Di Carlo D (2019). Enhanced In Vivo Delivery of Stem Cells using Microporous Annealed Particle Scaffolds. Small, 15(39), 1903147. 10.1002/smll.201903147

Li F, Truong VX, Fisch P, Levinson C, Glattauer V, Zenobi-Wong M, Thissen H, Forsythe JS, & Frith JE (2018). Cartilage tissue formation through assembly of microgels containing mesenchymal stem cells. Acta biomaterialia, 77, 48–62. [PubMed: 30006317]

Li K, Shen Y, Miller MA, Stabenow J, Williams RW, & Lu L (2021). Differing susceptibility of C57BL/6J and DBA/2J mice—parents of the murine BXD family, to severe acute respiratory syndrome coronavirus infection. Cell & Bioscience, 11(1), 1–6. [PubMed: 33407894]

Liu Y, Suarez-Arnedo A, Riley L, Miley T, & Segura T (2022a). Spatial confinement modulates macrophage response in microporous scaffolds. bioRxiv, 2022–2008.

Liu Y, Suarez-Arnedo A, Riley L, Miley T, & Segura T (2022b). Spatial confinement modulates macrophage response in microporous scaffolds. bioRxiv.

Liu Y, Suarez-Arnedo A, Shetty S, Schneider M, Collier JH, & Segura T (2022). A balance between pro-inflammatory and pro-reparative macrophages is observed in regenerative D-MAPS. bioRxiv.

Liu Y, Suarez-Arnedo A, Shetty S, Wu Y, Schneider M, Collier JH, & Segura T (2023). A Balance between Pro-Inflammatory and Pro-Reparative Macrophages is Observed in Regenerative D-MAPS [https://doi.org/10.1002/advs.202204882]. Advanced Science, n/a(n/a), 2204882. https://doi.org/10.1002/advs.202204882

Liu Y, Suarez-Arnedo A, Riley L, Miley T, Xia J, & Segura T (2023). Spatial Confinement Modulates Macrophage Response in Microporous Annealed Particle (MAP) Scaffolds. Advanced Healthcare Materials, 2300823.

Lowen JM, Bond GC, Griffin KH, Shimamoto NK, Thai VL, & Leach JK (2023). Multisized Photoannealable Microgels Regulate Cell Spreading, Aggregation, and Macrophage Phenotype through Microporous Void Space. Advanced Healthcare Materials, 2202239.

Lynn AD, Kyriakides TR, & Bryant SJ (2010). Characterization of the in vitro macrophage response and in vivo host response to poly(ethylene glycol)-based hydrogels. J Biomed Mater Res A, 93(3), 941–953. 10.1002/jbm.a.32595 [PubMed: 19708075]

Madden LR, Mortisen DJ, Sussman EM, Dupras SK, Fugate JA, Cuy JL, Hauch KD, Laflamme MA, Murry CE, & Ratner BD (2010). Proangiogenic scaffolds as functional templates for cardiac tissue engineering. Proc Natl Acad Sci U S A, 107(34), 15211–15216. 10.1073/pnas.1006442107 [PubMed: 20696917]

Margraf A, & Perretti M (2022). Immune cell plasticity in inflammation: Insights into description and regulation of immune cell phenotypes. Cells, 11(11), 1824. [PubMed: 35681519]

Marshall CD, Hu MS, Leavitt T, Barnes LA, Lorenz HP, & Longaker MT (2018). Cutaneous scarring: basic science, current treatments, and future directions. Advances in wound care, 7(2), 29–45. [PubMed: 29392092]

Masson-Meyers DS, Andrade TAM, Caetano GF, Guimaraes FR, Leite MN, Leite SN, & Frade MAC (2020). Experimental models and methods for cutaneous wound healing assessment. International journal of experimental pathology, 101(1–2), 21–37. [PubMed: 32227524]

Nichols SP, Koh A, Brown NL, Rose MB, Sun B, Slomberg DL, Riccio DA, Klitzman B, & Schoenfisch MH (2012). The effect of nitric oxide surface flux on the foreign body response to subcutaneous implants. Biomaterials, 33(27), 6305–6312. [PubMed: 22748919]

Orbach R, & Su X (2020). Surfing on membrane waves: Microvilli, curved membranes, and immune signaling. Frontiers in immunology, 11, 2187. [PubMed: 33013920]

Pruett L, Koehn H, Martz T, Churnin I, Ferrante S, Salopek L, Cottler P, Griffin DR, & Daniero JJ (2020). Development of a microporous annealed particle hydrogel for long-term vocal fold augmentation. The Laryngoscope, 130(10), 2432–2441. [PubMed: 31821567]

Qazi TH, Wu J, Muir VG, Weintraub S, Gullbrand SE, Lee D, Issadore D, & Burdick JA (2022). Anisotropic Rod-Shaped Particles Influence Injectable Granular Hydrogel Properties and Cell Invasion (Adv. Mater. 12/2022) [https://doi.org/10.1002/adma.202270092]. Advanced Materials, 34(12), 2270092. https://doi.org/10.1002/adma.202270092

Quintelier K, Couckuyt A, Emmaneel A, Aerts J, Saeys Y, & Van Gassen S (2021). Analyzing high-dimensional cytometry data using FlowSOM. Nature Protocols, 16(8), 3775–3801. 10.1038/s41596-021-00550-0 [PubMed: 34172973]

Rao VV, Wechsler ME, Cravens E, Wojda SJ, Caldwell AS, Kirkpatrick BE, Donahue SW, & Anseth KS (2022). Granular PEG hydrogels mediate osteoporotic MSC clustering via N-cadherin influencing the pro-resorptive bias of their secretory profile. Acta Biomaterialia, 145, 77–87. [PubMed: 35460910]

Riley L, Cheng P, & Segura T (2022). Void space and scaffold analysis of packed particles: applications in granular biomaterials.

Riley L, Schirmer L, & Segura T (2019). Granular hydrogels: emergent properties of jammed hydrogel microparticles and their applications in tissue repair and regeneration. Curr Opin Biotechnol, 60, 1–8. 10.1016/j.copbio.2018.11.001 [PubMed: 30481603]

Riley L, Wei G, Bao Y, Cheng P, Wilson KL, Liu Y, Gong Y, & Segura T (2022). Void volume fraction of granular scaffolds. Small, 2303466.

Rosengren A, & Bjursten LM (2003). Pore size in implanted polypropylene filters is critical for tissue organization. Journal of Biomedical Materials Research Part A, 67A(3), 918–926. 10.1002/jbm.a.10509

Schaffer BS, Grayson MH, Wortham JM, Kubicek CB, McCleish AT, Prajapati SI, Nelon LD, Brady MM, Jung I, & Hosoyama T (2010). Immune competency of a hairless mouse strain for improved preclinical studies in genetically engineered mice. Molecular cancer therapeutics, 9(8), 2354–2364. [PubMed: 20663932]

Seymour AJ, Shin S, & Heilshorn SC (2021). 3D printing of microgel scaffolds with tunable void fraction to promote cell infiltration. Advanced Healthcare Materials, 10(18), 2100644.

Sheikhi A, de Rutte J, Haghniaz R, Akouissi O, Sohrabi A, Di Carlo D, & Khademhosseini A (2019). Microfluidic-enabled bottom-up hydrogels from annealable naturally-derived protein microbeads. Biomaterials, 192, 560–568. [PubMed: 30530245]

Sussman EM, Halpin MC, Muster J, Moon RT, & Ratner BD (2014). Porous implants modulate healing and induce shifts in local macrophage polarization in the foreign body reaction. Ann Biomed Eng, 42(7), 1508–1516. 10.1007/s10439-013-0933-0 [PubMed: 24248559]

Suturin AC, Krüger AJD, Neidig K, Klos N, Dolfen N, Bund M, Gronemann T, Sebers R, Manukanc A, & Yazdani G (2022). Annealing High Aspect Ratio Microgels into Macroporous 3D Scaffolds Allows for Higher Porosities and Effective Cell Migration. Advanced Healthcare Materials, 2200989.

Szondi DC, Wong JK, Vardy LA, & Cruickshank SM (2021). Arginase signalling as a key player in chronic wound pathophysiology and healing. Frontiers in Molecular Biosciences, 1049.

Veiseh O, Doloff JC, Ma M, Vegas AJ, Tam HH, Bader AR, Li J, Langan E, Wyckoff J, & Loo WS (2015). Size-and shape-dependent foreign body immune response to materials implanted in rodents and non-human primates. Nature materials, 14(6), 643–651. [PubMed: 25985456]

Wang Z, Cui Y, Wang J, Yang X, Wu Y, Wang K, Gao X, Li D, Li Y, Zheng X-L, Zhu Y, Kong D, & Zhao Q (2014). The effect of thick fibers and large pores of electrospun poly(ε-caprolactone) vascular grafts on macrophage polarization and arterial regeneration. Biomaterials, 35(22), 5700–5710. https://doi.org/10.1016/j.biomaterials.2014.03.078 [PubMed: 24746961]

Widener AE, Roberts A, & Phelps EA Single versus dual microgel species for forming guest-host microporous annealed particle PEG-MAL hydrogel. Journal of Biomedical Materials Research Part A.

Xin S, Chimene D, Garza JE, Gaharwar AK, & Alge DL (2019). Clickable PEG hydrogel microspheres as building blocks for 3D bioprinting. Biomaterials science, 7(3), 1179–1187. [PubMed: 30656307]

Xin S, Wyman OM, & Alge DL (2018). Assembly of PEG Microgels into Porous Cell-Instructive 3D Scaffolds via Thiol-Ene Click Chemistry [https://doi.org/10.1002/adhm.201800160]. Advanced Healthcare Materials, 7(11), 1800160. https://doi.org/10.1002/adhm.201800160

Xue M, & Jackson CJ (2015). Extracellular Matrix Reorganization During Wound Healing and Its Impact on Abnormal Scarring. Advances in wound care, 4(3), 119–136. 10.1089/wound.2013.0485 [PubMed: 25785236]

Yin Y, He X-T, Wang J, Wu R-X, Xu X-Y, Hong Y-L, Tian B-M, & Chen F-M (2020). Pore size-mediated macrophage M1-to-M2 transition influences new vessel formation within the compartment of a scaffold. Applied Materials Today, 18, 100466. 10.1016/j.apmt.2019.100466

Zhu S, Li S, Escuin-Ordinas H, Dimatteo R, Xi W, Ribas A, & Segura T (2018). Accelerated wound healing by injectable star poly(ethylene glycol)-b-poly(propylene sulfide) scaffolds loaded with poorly water-soluble drugs. J Control Release, 282, 156–165. 10.1016/j.jconrel.2018.05.006 [PubMed: 29751029]

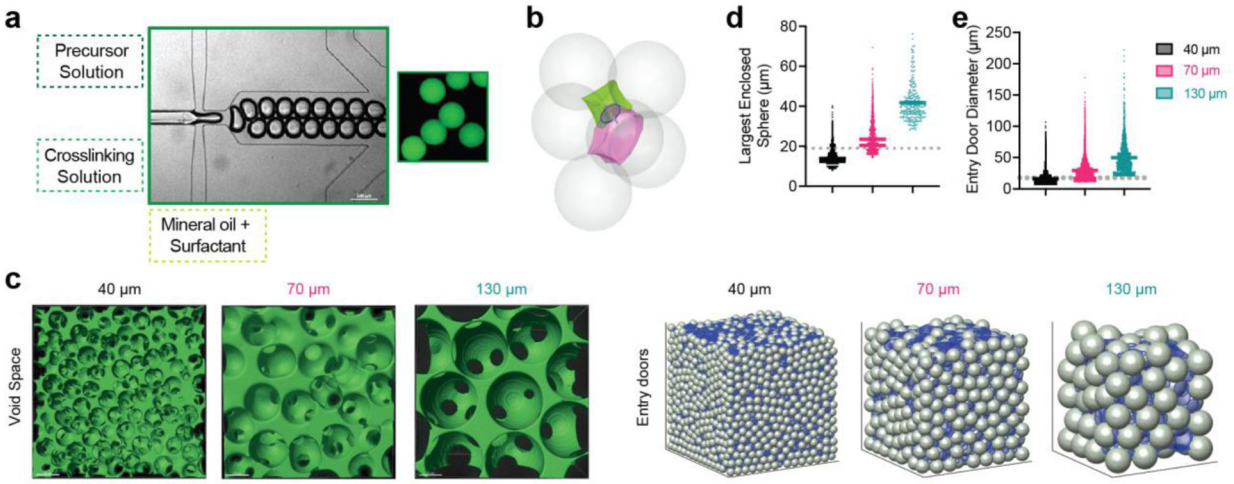

Figure 1.

40 μm, 70 μm, and 130 μm MAP scaffolds were chemically and mechanically identical. a, scheme illustrating microgel formation using a microfluidic water-in-oil emulsion system. A precursor solution and a crosslinker solution are fused and segmented into droplets, which are then crosslinked into microgels via Michael addition. b, sample green and pink 3D-pores separated by a door (blue circle) and surrounded by six microgels. c, (Left) fluorescent images showing void space; (Right) entry doors (blue circles) for 40 μm, 70 μm, and 130 μm simulated MAP scaffolds. d, the diameter of the largest enclosed sphere within each 3D-pore for simulated 40 μm, 70 μm, and 130 μm MAP scaffolds compared to the diameter of bone marrow-derived macrophages (BMDM) in 3D culture (grey dotted line). e, the diameters of all entry doors for simulated 40 μm, 70 μm, and 130 μm MAP scaffolds compared to the diameter of BMDM in 3D culture (grey dotted line). Statistical analysis: one-way ANOVA.

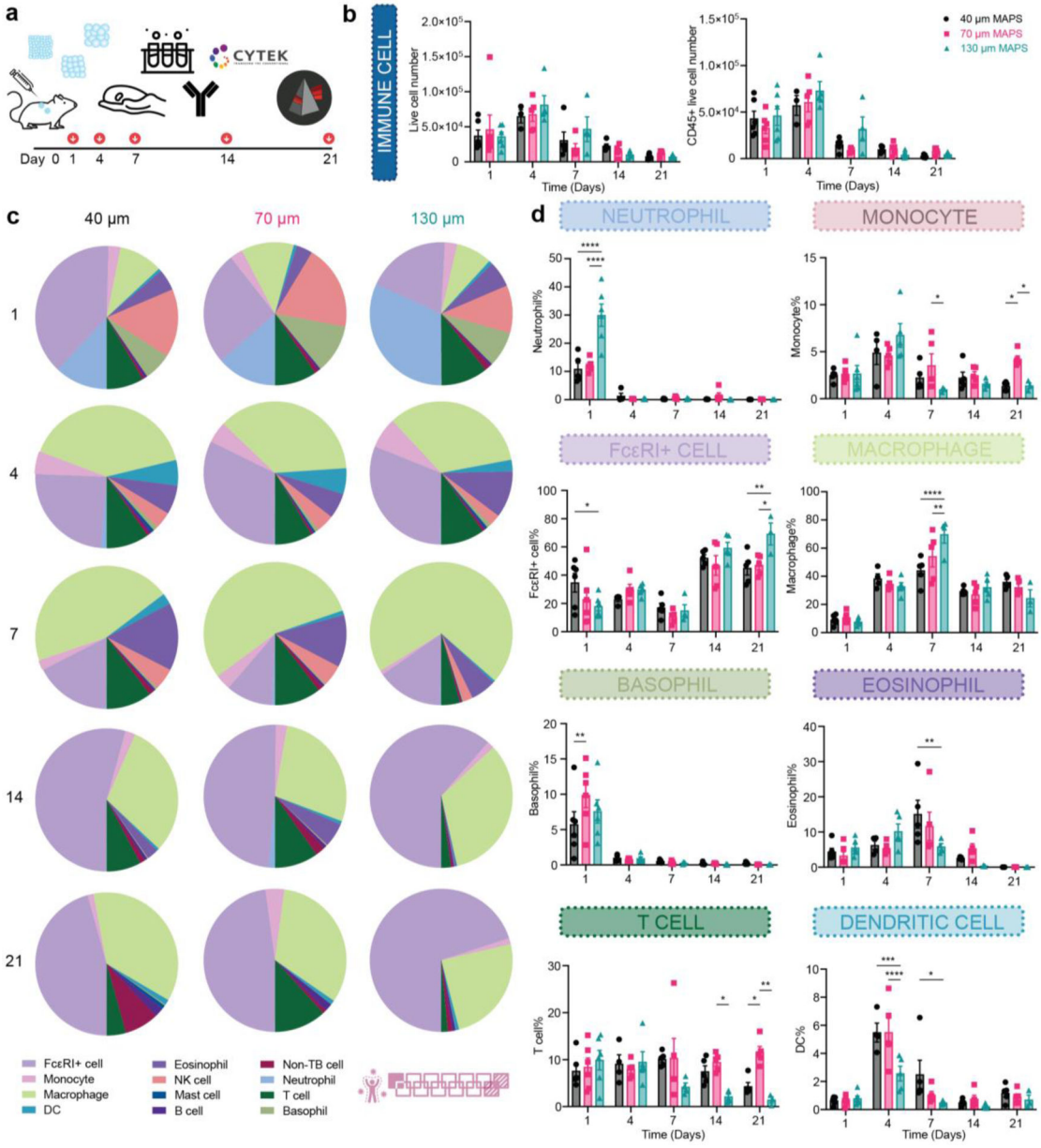

Figure 2.

Immune cell recruitment and response followed a size-dependent manner in the subcutaneous implantation model. a, Scheme illustrating the experiment timeline. After the initial injections, implant extraction and flow cytometry were performed at designated time points (days 1, 4, 7, 14, 21). b, the total number of live cells (Zombie NIR-) and CD45+ immune cells (CD45+). c, pie charts of myeloid cell abundancy across 5 time points for 40 μm, 70 μm, and 130 μm MAP scaffolds. Each number was an average of the results from 5 mice. d, neutrophil, monocyte, FcεRI+ cell, macrophage, Basophil, eosinophil, T cell and dendritic cell percentages among all CD45+ live cells. Statistical analysis: two-way ANOVA with Šídák's multiple comparisons test made between 40 μm, 70 μm, and 130 μm MAP scaffolds groups only when there was a significance in the interaction term of scaffold type

x time. * p<0.05, ** p<0.01, *** p<0.001, **** p<0.0001. Error bars, mean ± s.e.m., n = 6 mice per group for day 1 and n = 5 mice per group for the other time points. The pink symbol in the middle bottom of the graph stands for the 13-color innate cell panel used in this figure.

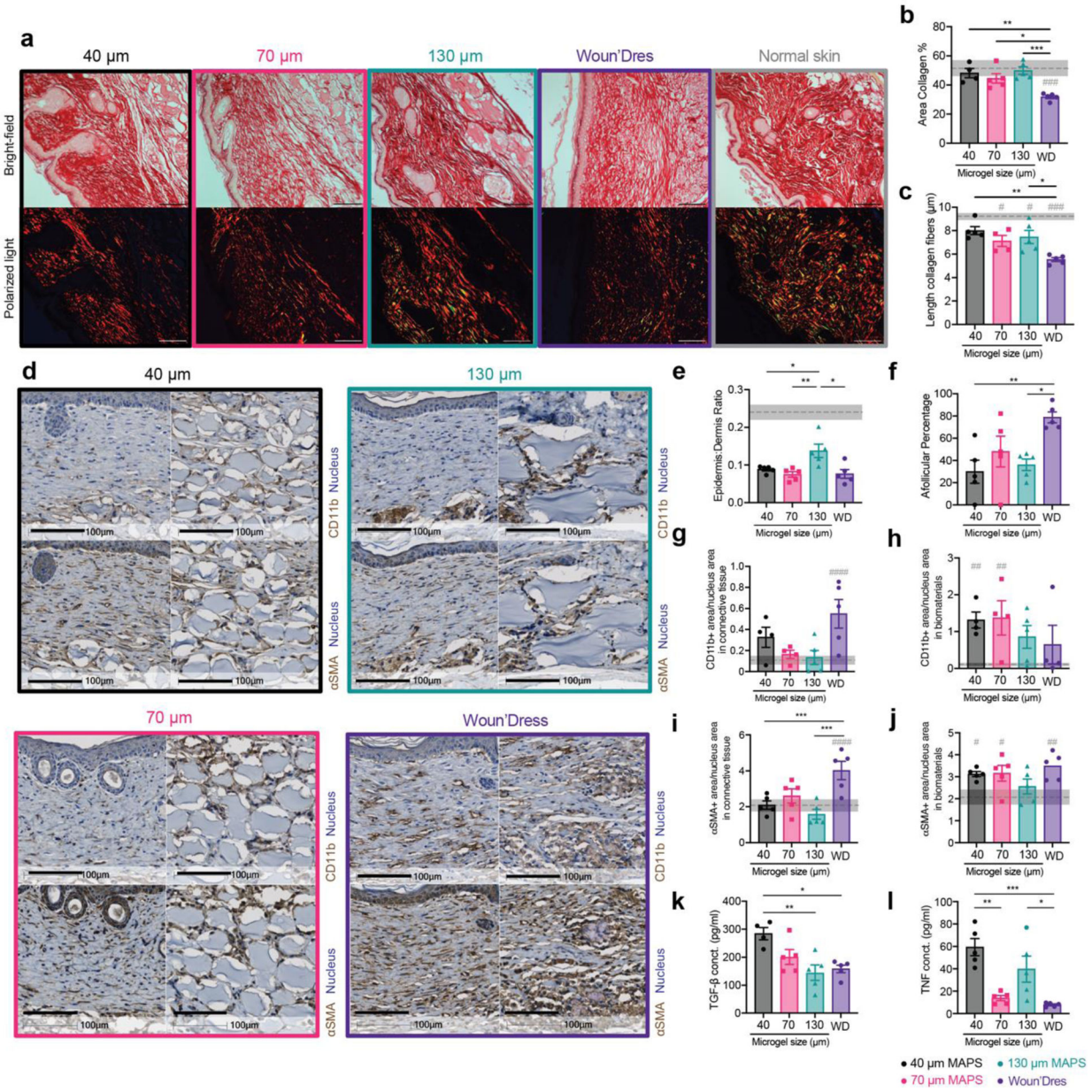

Figure 3.

130 μm MAP scaffolds induced mature collagen regeneration and reduced inflammation level in the skin wound. a, representative pictures of 21-day skin wound samples with Picro-Sirius Red staining (top row, bright field image, scale bar, 100 μm; bottom row, image with polarized light, scale bar, 100 μm). b, percentage of collagen (bright field area) in the regions of interest. c, average length of collagen fibers in the regions of interest. d, representative pictures of 21-day skin wound samples with immunohistochemical staining of CD11b and α-SMA (left: connective tissue in the wound bed, scale bar, 100 μm; right: remaining biomaterials, scale bar, 100 μm). e, the ratio of epidermis thickness to dermis thickness. The dotted line and the grey area stand for the average number and the range for normal skin. f, afollicular percentage in the wound bed. g-h, the percentage of CD11b+ area

as a ratio of the nucleus area in the connective tissue and in the remaining biomaterials. i-j, the percentage of α-SMA + area as a ratio of the nucleus area in the connective tissue and in the remaining biomaterials. k-l, ELISA results of TGF-β and TNF concentrations in MAP-treated wounds 21 days post-wounding. Statistical analysis: two-way ANOVA with Šídák's multiple comparisons test made between treatment groups only when there was a significance in the interaction term of treatment type x time. Dunnet method was used to compare each treatment against normal skin baseline (gray pond). */# $p < 0.05$, **/## $p < 0.001$, *** $p < 0.001$, ****/#### $p < 0.0001$. Error bars, mean ± s.e.m., n = 5 mice per group with some data points removed due to experimental reasons.

Figure 4.

Immune cell recruitment and response followed a size-dependent manner in the wound healing model. a, Scheme illustrating the experiment timeline. After the initial wounding and biomaterial treatment, skin extraction and flow cytometry were performed at designated time points (days 1, 7, 21). b, the total number of live cells (Zombie NIR-) and CD45+ immune cells across three time points. c, pie charts of myeloid cell abundancy across 3 time points for 40 μm, 70 μm, and 130 μm MAP scaffolds. Each number was an average of the results from 5 mice. d, neutrophil, monocyte, FcεRI+ cell, macrophage, basophil, T cell, B cell, Natural killers (NK) cell percentages among all CD45+ live cells. Statistical analysis: two-way ANOVA with Šídák's multiple comparisons test made between 40 μm, 70 μm, and 130 μm MAP scaffolds and wound dressing groups only when there was a significance in the interaction term of scaffold type x time. * $p<0.05$, ** $p<0.01$, *** $p<0.001$, ****

$p<0.0001$. Error bars, mean ± s.e.m., n = 5 mice per group. The pink symbol in the middle right of the graph stands for the 13-color innate cell panel used in this figure.

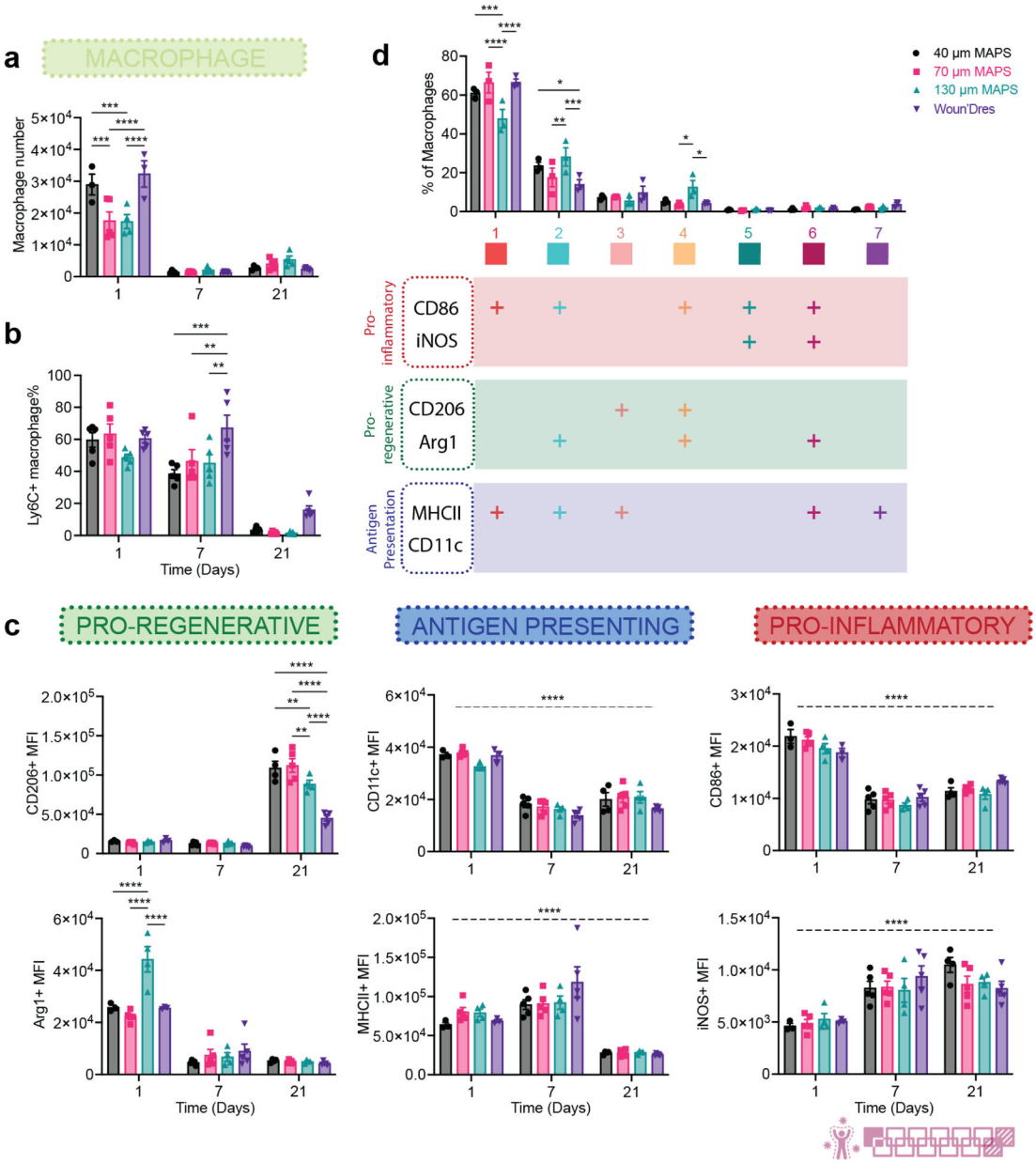

Figure 5.

130 μm MAP scaffolds modulated a timely transition in pro-regenerative macrophage phenotypes. a, the number of macrophages in total live cells across 3 time points. b, Ly6C+ macrophage percentage in total macrophages. c, MFI of CD206, Arg1, CD11c, MHCII, CD86, and iNOS in total macrophage population over time. d, tSNE clustering of macrophages in MAP scaffolds-treated wounds on day 1. The bar graph showed the percentages each sub-population took up in the total macrophage population. The table beneath it showed the expression levels of each marker in 7 different macrophage populations. "+" indicates that more than 50% of the population expressed that marker. Statistical analysis: two-way ANOVA with Šídák's multiple comparisons test made between 40 μm, 70 μm, and 130 μm MAP scaffolds and wound dressing groups only when there

was a significance in the interaction term of scaffold type x time. * $p<0.05$, ** $p<0.01$, *** $p<0.001$, **** $p<0.0001$. Asterisks with solid line stand for comparisons between groups. Asterisks with dash line stand for significance in time. Error bars, mean ± s.e.m., n = 5 mice per group. The pink symbol in the bottom right corner of the graph stands for the 13-color innate panel used in this figure.

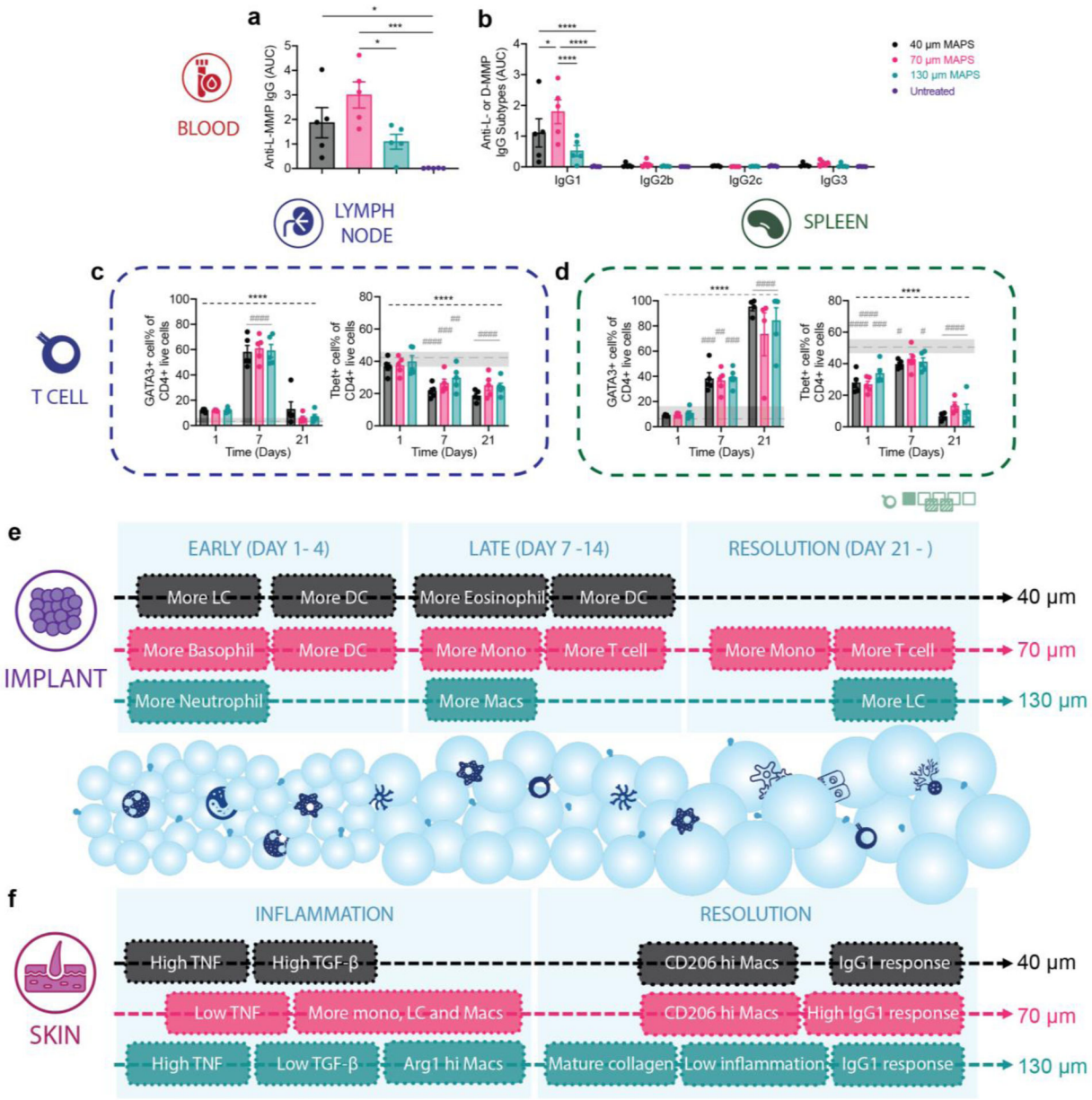

Figure 6.

A pro-reparative IgG1-biased Th2 response was observed in 70 µm MAP scaffolds. a and b, ELISA results of total anti-L-MMP (peptide crosslinker) IgG level and the anti-L-MMP IgG subtypes in mice treated with 40 µm, 70 µm, and 130 µm MAP scaffolds after 21 days. c and d, T cell profiles in draining lymph nodes and spleen of mice treated with 40 µm, 70 µm, and 130 µm MAP scaffolds across 3 time points. e and f, schematic illustrations of the immune responses to 40 µm, 70 µm, and 130 µm MAP scaffolds in the subcutaneous implantation model and the wound healing model. Statistical analysis: two-way ANOVA with Šídák's multiple comparisons test made between 40 µm, 70 µm, and 130 µm MAP scaffolds groups only when there was a significance in the interaction term of scaffold type x time. After a two-way ANOVA, Dunnet method was used to compare the experiment groups with the

baseline control group. * $p<0.05$, ** $p<0.01$, *** $p<0.001$, **** $p<0.0001$. Asterisks with solid line stand for comparisons between MAP scaffolds. Asterisks with dash line stand for significance in time. Error bars, mean ± s.e.m., n = 5 mice per group but with some data points removed due to experimental reasons. The green symbol beneath panel d stands for the 7-color T cell panel used in panel c, d of this figure.